

The Ground Station High-Power Traveling-Wave Tube

By R. J. COLLIER, G. D. HELM, J. P. LAICO and K. M. STRINY

(Manuscript received February 27, 1963)

The M4040 is a 2-kw CW traveling-wave tube developed specifically for communications applications. It was used as the power amplifier in the Project Telstar ground transmitter. Analytic methods employed in the design of the electron gun, the beam collector, the RF circuit and the output match are presented. Typical performance characteristics and drawings of the tube subassemblies serve to describe the electrical and physical features of the M4040 traveling-wave tube. Methods used to inhibit oscillation and the effects of ion drainage and collector depression on tube performance are also discussed.

I. INTRODUCTION

This paper describes the design of the M4040 2-kw CW traveling-wave tube amplifier which was developed specifically for communications applications. It was used as the final power amplifier in the Telstar transmitters at Andover, Maine, and Pleumeur-Bodou, France. It was necessary for the Telstar amplifier to meet the requirements shown in Table I.

The M4040 was designed to have sufficient instantaneous bandwidth to operate anywhere in the communications band from 5.925 to 6.425 gc. The design approach was a conservative one aimed primarily at delivering an operable tube in time for the Telstar experiment. The development time was approximately 18 months. In describing the M4040, we shall discuss only briefly its mechanical aspects. The prime intent is to present electrical design and operating information which may be applicable to future high-power traveling-wave tube development. Topics concerned with the electrical design of the electron gun, the beam collector, and the slow-wave structure will be discussed. Finally, some performance characteristics will be presented, accompanied by comments on the tube operation.

TABLE I — REQUIREMENTS

Output power (maximum)	2 kw CW
Small-signal gain	30 db
Large-signal gain	27 db
Bandwidth	25 mc
Center operating frequency	6.39 gc
Output amplitude ripple (small signal)	± 0.5 db
Input signal amplitude range	30 db

II. GENERAL DESCRIPTION OF THE M4040

The M4040 is an all metal and ceramic electron tube 4 feet in length, 17 inches in diameter, and 230 pounds in weight. These dimensions include an aluminum foil solenoid which produces an axial beam-focusing field of 730 gauss along the 13 inches of slow-wave circuit. The electron gun is magnetically shielded, as is the solenoid and collector. The gun is a Pierce convergent type. The slow-wave circuit is a coupled-cavity structure with coupling slots rotated by 180° in each successive cavity. A single sever is employed. The sever attenuators are located in short waveguides matched to the circuit but are still in the vacuum. Microwave power is fed into and coupled out of the tube through ceramic windows, step transformers, narrow-height guide and matching cavities which form part of the slow-wave structure. The beam diverges into the beam collector under the action of space-charge forces alone. The slow-wave structure, solenoid and beam collector are separately water-cooled. Fig. 1 is a photograph of the M4040 located in the solenoid. The appendage ion pumps shown in the figure continuously pump the tube at the gun, as well as at the collector end. In the picture, the collector is at the top and the gun is at the bottom.

Fig. 2 is a cutaway section. Axial alignment of the tube in the magnetic field is preplumbed, and no adjustments are necessary to optimize their relationship. Figs. 3 to 7 are sketches showing more detail of the tube construction: respectively, the gun, RF circuit, collector, sever, and coupling assemblies. The construction materials are typical of those used in electron devices in that they have low vapor pressures and can withstand vigorous cleaning and the heating associated with outgassing. The residual gas pressure in a sealed-off M4040 is less than 1×10^{-8} torr. The tube is outgassed by heating, not only when the tube is finally processed, but also in the subassembly stages indicated in substance by Figs. 3 to 7, inclusive.

The gun shown in Fig. 3 is made of molybdenum, tungsten, and ceramic parts welded, brazed or glazed together. The spacing of the beam-forming electrode to the cathode is held to ± 0.0003 inch, and the



Fig. 1 — The M4040 traveling-wave tube.

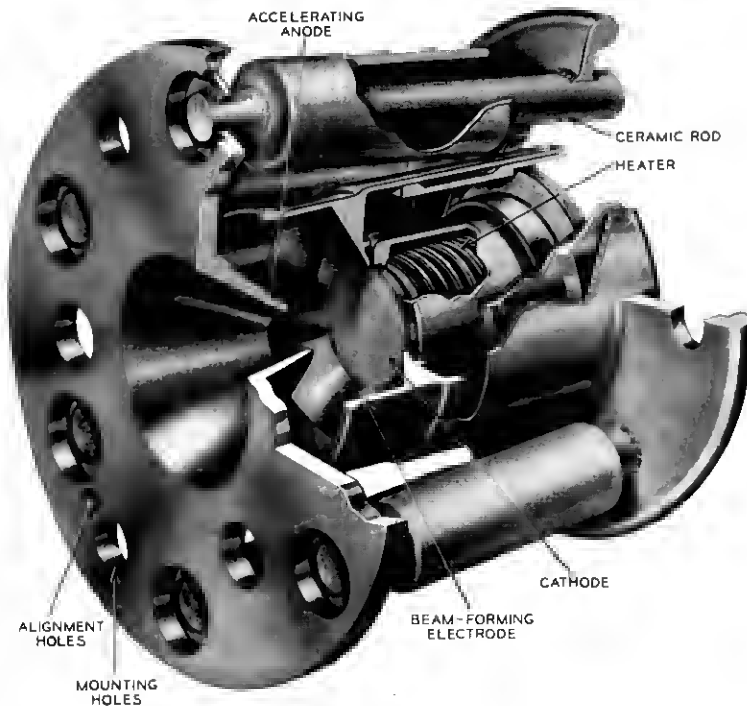


Fig. 3 — M4040 electron gun.

concentricity of these with respect to each other and to the accelerating anode is held to ± 0.001 inch. Six Alsimag 475 insulators support and electrically isolate the accelerating anode from the cathode and the beam-forming electrode so as to safely withstand 18,000 volts. Re-entrant skirts are an integral part of these insulators and insure against electrical leakage arising from the deposition of metallic vapors emanating principally from the cathode; the latter is a Phillips Metallonics type B tungsten matrix cathode.

The RF structure identified in Fig. 4 consists of a stack of 29 copper cavities capped at each end by a steel pole-piece and machined at its center to provide for the addition of the sever sections. Adjacent to each steel pole-piece is the input or output waveguide, respectively. In each cavity and pole-piece, holes or channels are machined so that when the parts are finally brazed together, they not only form the RF circuit but also provide the path for circulating cooling water. The brazed assembly

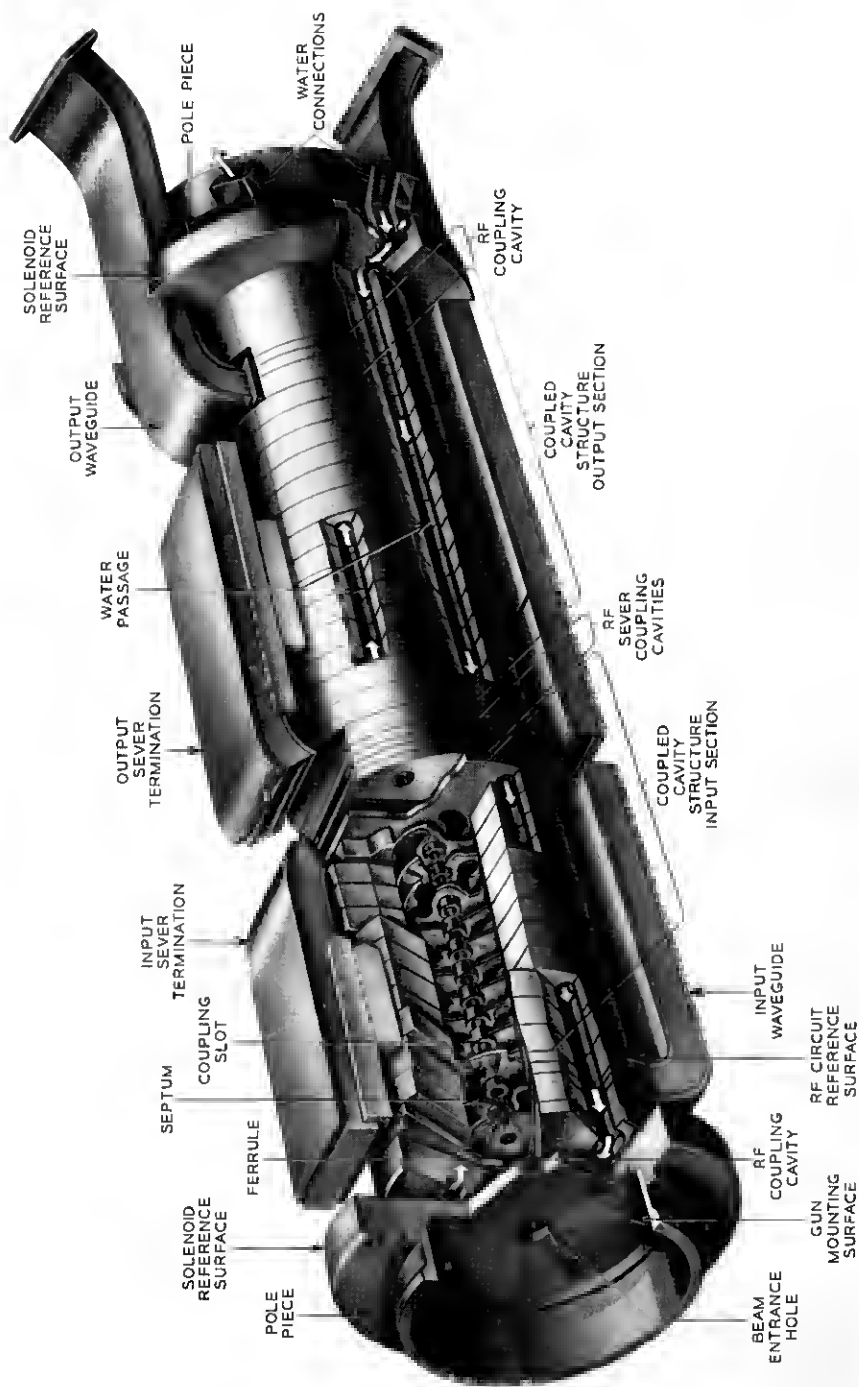


Fig. 4 — M4040 RF circuit.

meets the concentricity requirement of 0.004 inch on all central holes with respect to each other and to the outside diameter of the pole-pieces. After auxiliary subassemblies such as the sever sections and waveguides are assembled, the unit is outgassed by heating to about 500°C until a pressure of 5×10^{-6} torr is achieved.

In Fig. 5 the collector subassembly is shown. This is a set of concentric tubes of copper and steel to provide, in addition to the beam collector cavity, an annular channel for the passage of cooling water at the rate of 18 gpm. The collector is electrically isolated from the body of the tube by a ceramic insulator, allowing any beam current intercepted by the slow-wave structure to be monitored.

A sever section subassembly is shown in Fig. 6. A significant feature of this unit is the carbonized ceramic attenuator, which is a wedge of porous alumina 0.156×1.372 inches at one end and tapering to a point at the other end. To aid in dissipating some 300 watts of unwanted power, it is brazed to a molybdenum base plate. One surface of the ceramic is metallized with standard molybdenum manganese powder mixture in the empirically determined pattern shown in Fig. 6. Carbonizing is accomplished by soaking the unit in sugar solution and then converting the sugar to carbon by heating to 900°C in a purified dry hydrogen atmosphere.

The RF coupling assembly shown in Fig. 7 is the same for the input and output. It contains a step transformer section and an RF window which also forms part of the vacuum wall. The metal member of this vacuum seal is especially designed to provide sufficient elasticity to compensate for the mismatch in expansion between it and the ceramic and to better withstand thermal shocks.

An electrical description of the M4040 is furnished by Tables II, III and IV.

III. VOLTAGE SCALING OF AN ELECTRON GUN

To minimize development time, it was decided to scale in voltage a gun whose properties were previously measured at 1000 volts. We were able to predict the beam minimum radius and perveance quite successfully, enabling work on the slow-wave circuit to progress in parallel with the gun measurements program. The measurements of the beam cylindrical symmetry and the beam profile as a function of voltage and of distance from a reference surface on the beam-forming electrode were performed using the "pin-hole collector" technique.

Figs. 8(a) and 8(b) present measurements of the beam minimum radius and its location as a function of voltage. The radius is taken as

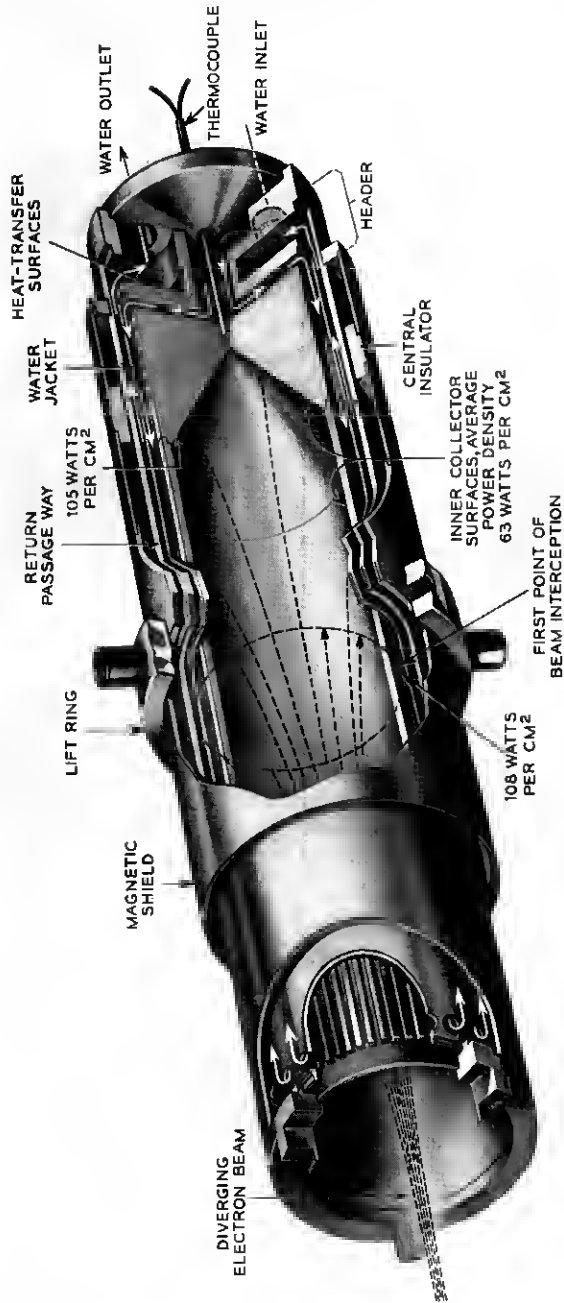


Fig. 5 — M4040 collector.

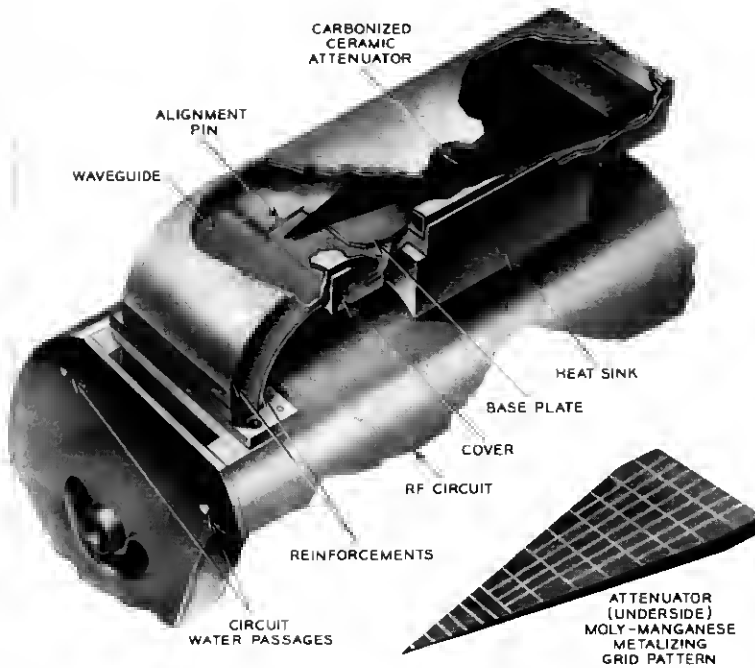


Fig. 6 — M4040 sever termination.

that which encloses 95 per cent of the total current. If the thermal motion of the electrons is neglected, these quantities are theoretically constant and are given by the curves labeled "universal beam spread." The latter were calculated by the methods described in Pierce¹ but with an additional correction for the focal length of the anode-aperture lens given by $F = 1.1$, where F is defined as in Danielson, Rosenfeld and Saloom.² On the other hand, transverse thermal velocities of the electrons cause the beam minimum radius to be smaller and closer to the cathode than predicted by the universal beam spread curve.

Danielson, Rosenfeld and Saloom have devised a theory which predicts the size and location of the beam minimum radius as a function of voltage and cathode temperature for several values of perveance. Their results were generalized by Herrmann³ who presented curves having a wider applicability. The results predicted by Herrmann are shown in Figs. 8(a) and 8(b) for comparison with the experimental data and the universal beam spread values.

Fig. 8(a) suggests that a useful rule to apply when predicting the

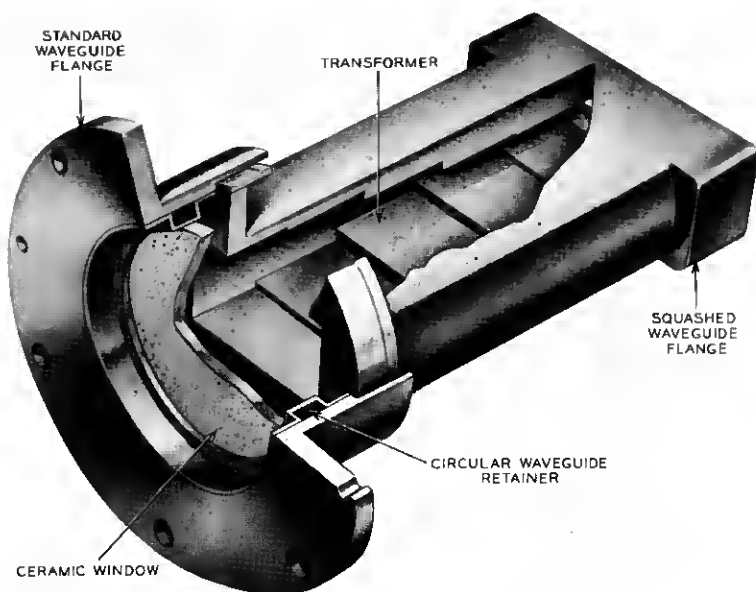


Fig. 7 — M4040 RF window assembly.

beam properties of an electron gun at a scaled voltage is that the theoretical behavior is given by the Herrmann curves up to the voltage at which they intersect the universal beam spread values and by the latter quantities at higher voltages. In comparing theory and experiment, we note that the experimental beam minimum radius is larger by 10 to 20 per cent, and its location falls within 10 per cent of the expected distance from the cathode.

TABLE II — ELECTRICAL DESIGN PARAMETERS AT MIDBAND

Midband frequency	6.15 gc
Gun perveance	0.47×10^{-6} amp/(volts) ¹
Gain parameter, C	0.062
Space charge parameter, QC	0.3
(Radial phase constant) \times (beam radius), γr_b	0.65
Growing wave parameter, X	0.65
Velocity parameter, b	1.0
No. of beam wavelengths, N	20
No. of active cavities	29
Beam radius (r_{95}), r_b	0.049 inch
Tunnel radius, a	0.082 inch
Cathode radius, r_c	0.205 inch

TABLE III — TYPICAL CHARACTERISTICS FOR M4040
OPERATED IN THE *Telstar* GROUND STATION

(a) Input	
Cathode potential	-17,000 v
Accelerator potential	+600 v
Circuit potential	0 v
Collector potential	0 v
Heater current	6.2 amps
Heater voltage	7.25 v
Solenoid current	23 amps
Solenoid voltage	15.3 v
Total cathode emission current	1030 ma
Collector water flow rate	18 gal/min
Circuit water flow rate	3.5 gal/min
Solenoid water flow rate	0.5 gal/min
Maximum signal power	3 watts
(b) Output	
Rated frequency range	6.35-6.45 gc
Rated maximum output power	2000 watts
Small-signal gain	31.8-30.8 db
Output amplitude ripple	± 0.2 db
Gain at 2000-watt level	28 db
Magnetic field	730 oersted
Circuit interception current (no drive)	4 ma
Circuit interception current (with drive)	35 ma
Accelerator interception current	0.1 ma

TABLE IV — TYPICAL M4040 CHARACTERISTICS
FOR BROADBAND HIGH-POWER OPERATION

(a) Input	
Cathode potential	-17,400 v
Total cathode emission current	1040 ma
Signal power	≈ 4 watts
(Other values are the same as in Table IIIa)	
(b) Output	
Center frequency, f_0	≈ 6.15 gc
Output power at center frequency	2500 watts
Gain at f_0 and at 2500-watt level	28 db
1-db instantaneous bandwidth (i.e., band edge power = 2 kw)	$12.7\% = 780$ me
Efficiency at f_0	13.8%

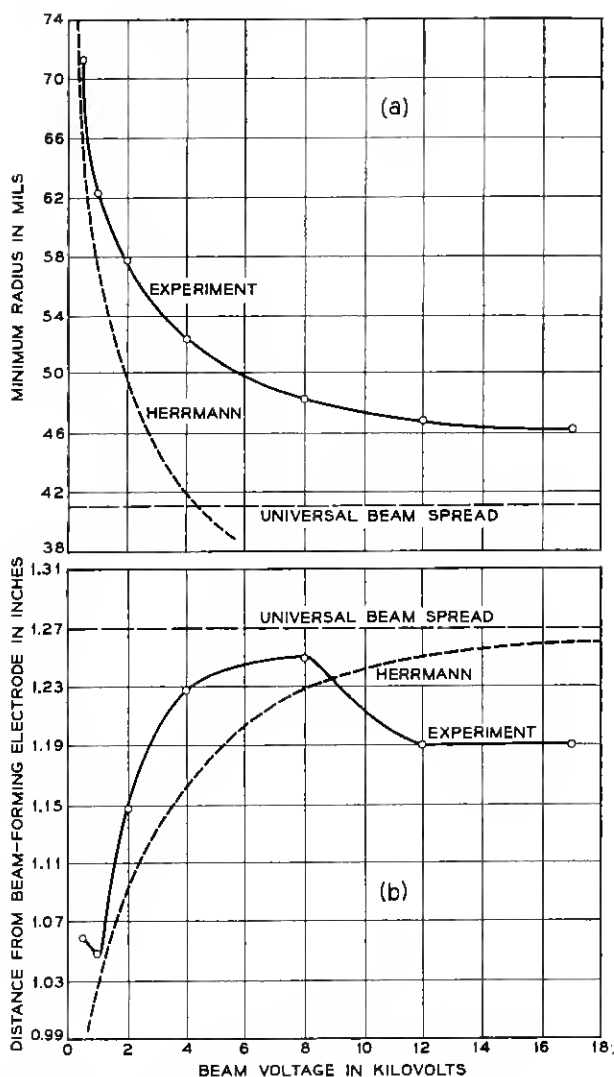


Fig. 8 — (a) Minimum beam radius (95 per cent of total current) vs beam voltage; (b) position of beam minimum vs voltage.

IV. DISTRIBUTION OF BEAM POWER IN THE COLLECTOR

If size and weight are of little consequence, the beam collector of a traveling-wave tube should be designed to minimize temperature inside the vacuum. Let us consider the spread of a monovelocity, homogeneous beam into an ideal hard-vacuum, field-free region. The universal beam

spread curve referred to in the previous section has been derived by several authors.^{1,4} The relation between the axial distance the beam has drifted and the beam radius can be written as

$$z = \frac{r_0 Z}{\sqrt{K}} \quad (1)$$

where r_0 is the beam radius on entering the field-free region and

$$K = \frac{I}{V^{3/2}} \cdot \left(\frac{m}{e}\right)^{1/2} \cdot \frac{1}{2\sqrt{2\pi\epsilon_0}}. \quad (2)$$

The beam radius r_b appears in the expression for Z , viz.

$$Z = \int^t 2e^{t^2} dt \quad (3)$$

where $t = \sqrt{\ln R}$, in the form of a normalized radius $R = r_b/r_0$. The half-value of the integral in (3) is tabulated by Jahnke and Emde⁵ for various values of t . One can plot the normalized radius R against the normalized axial distance Z to obtain the "universal beam spread curve." Applying the specific values of the normalizing constants associated with the M4040, we plot in Fig. 9 r_b versus z . Also plotted in

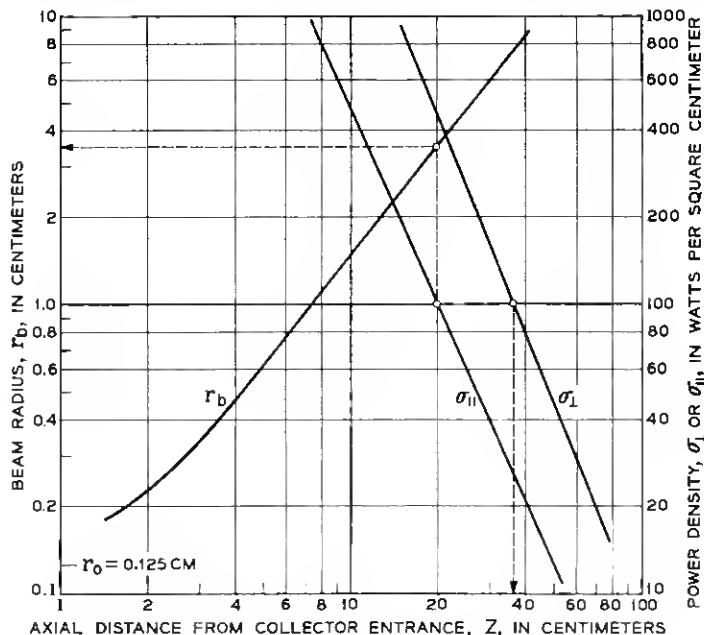


Fig. 9 — M4040 collector design chart.

Fig. 9 is the power density incident on a surface normal to the beam axis, σ_{\perp} , whose value is obtained for any value of z by dividing the total beam power by the area of a circle whose radius is read from the r_b versus z plot. The M4040 has been designed with a total beam power of about 17.7 kw so that the power density at the minimum radius of the beam ($r_0 \approx 0.125$ cm) is $\sigma_{\perp} \approx 360$ kw/cm².

If it is assumed that the collector is cylindrical in shape, the power density incident on a surface parallel to the beam axis, σ_{\parallel} , will be of interest. Consider the beam to be spreading such that the edge electrons make an angle φ with the initial beam axis. Then the power illuminating a small area, A_{\perp} , which is located at the beam edge and is perpendicular to the initial beam axis, is given by $\sigma_{\perp} A_{\perp}$. When A_{\perp} is projected by the beam illumination onto the surface parallel to the initial beam axis, it takes the value A_{\parallel} such that

$$\frac{A_{\perp}}{A_{\parallel}} = \tan \varphi = \frac{dr_b}{dz} = r_b' \quad (4)$$

Equating the power incident on A_{\perp} to that on A_{\parallel}

$$\sigma_{\perp} A_{\perp} = \sigma_{\parallel} A_{\parallel} \quad (5)$$

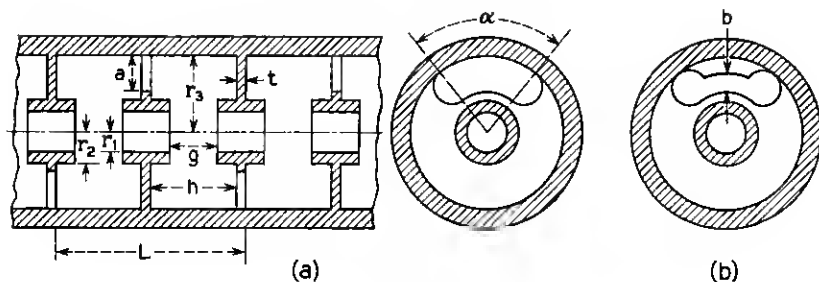
where σ_{\parallel} is the power in the beam edge incident on a square unit area parallel to the initial beam axis. Upon the substitution of (4) into (5), we find that

$$\sigma_{\parallel} = \sigma_{\perp} r_b' = \sigma_{\perp} \sqrt{K} \sqrt{\ln r_b/r_0} \quad (6)$$

The expression for r_b' is obtained in deriving (1). σ_{\parallel} is plotted as a function of z in Fig. 9. Note that the interception of the beam edge on the cylindrical walls of the collector corresponds to the highest power density incident on those walls, since $\tan \varphi$ becomes smaller for all other conditions. Therefore, the collector may be designed such that the cylinder length determines when σ_{\perp} equals the maximum desired and the cylinder radius determines the same value for σ_{\parallel} . The length and radius corresponding to a power density of 100 watts/cm² are indicated on Fig. 9 for the M4040. This chart indicates the hottest spots. The power density on the side wall will average to the order of half σ_{\parallel} .

V. ANALYTICAL METHODS FOR DESIGNING AND MATCHING THE SLOW-WAVE CIRCUIT

Fig. 4, the sketch of the RF circuit, indicates that a relatively rugged, easily fabricated slow-wave structure can be formed from an induc-



SUMMARY OF M4040 CIRCUIT DIMENSIONS

a	0.325"	r_1	0.082"
b	0.1825"	r_2	0.122"
g	0.116"	r_3	0.5235"
h	0.294"	L	0.666"
t	0.040"	α	75°

Fig. 10 — (a) Slow-wave circuit dimensions showing unloaded coupling iris; (b) septum with a loaded coupling iris.

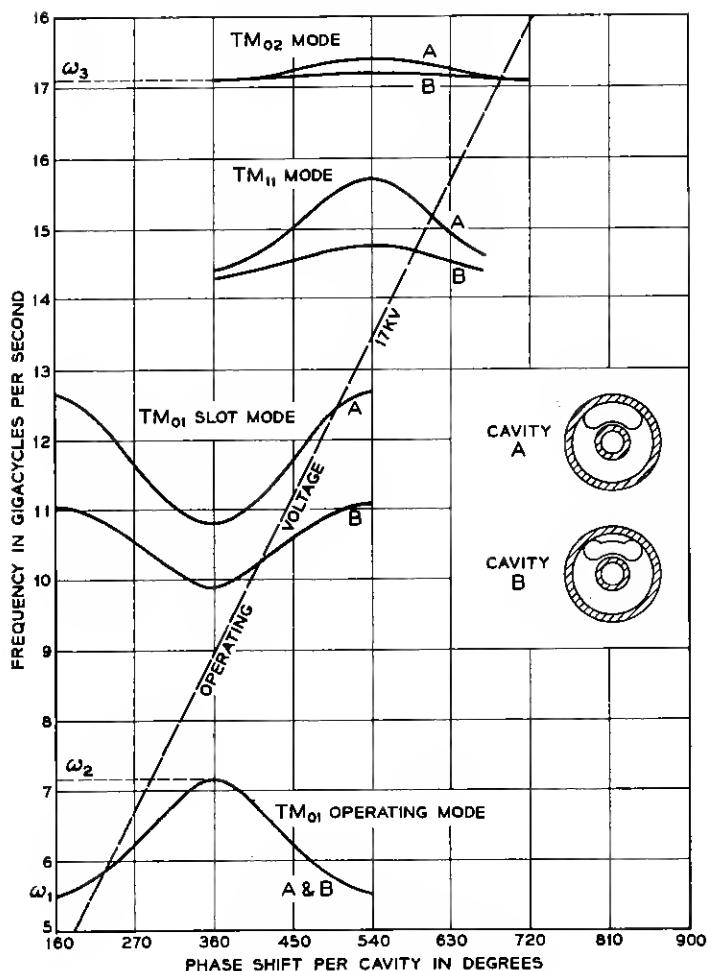
tively coupled chain of cylindrical cavities. Excellent heat dissipation properties are combined with a good impedance-bandwidth product. The important dimensional parameters are designated in Fig. 10; the parameter labels are those used in the analysis below.

ω - β diagrams for the four lowest modes are shown in Fig. 11. The M4040 is designed to operate on the first forward wave space harmonic of the TM_{01} cavity mode. Where the resonant frequency, ω_s , of the coupling slot is appreciably higher than the upper cutoff frequency, ω_2 , of the cavity, the dispersion curve of the TM_{01} cavity mode may be approximated by the equation

$$\cos\left(\frac{\beta L}{2}\right) = 1 - 2 \frac{\left[\frac{1}{\omega^2} - \frac{1}{\omega_2^2}\right]}{\left[\frac{1}{\omega_1^2} - \frac{1}{\omega_2^2}\right]}. \quad (7)$$

Here ω_1 is the lower cutoff frequency of the mode and L is the periodic length of the circuit.

The choice of the electron gun design establishes the electron beam radius, r_b , and the beam velocity, u_0 . These in turn determine the cavity beam hole radius $r_1 \approx 1.67 r_b$ and the periodic length $L \approx 3\pi u_0/\omega_0$,

Fig. 11 — ω - β diagrams.

where ω_0 is the synchronous frequency. The gap, g , between the ferrules capacitively loading the cylindrical cavities, is used to optimize the interaction impedance of the forward wave space harmonic. To this effect the gap-to-period ratio g/L is selected to lie between 0.1 and 0.2. The outer radius of the ferrule, r_2 , and the septum thickness, t , are designed to be as small as possible consistent with the heat energy to be dissipated.

Following Ramo and Whinnery,⁶ the cavity may be analyzed as a

foreshortened radial line resonator. The major cavity radius, r_3 , which sets the upper cutoff frequency, ω_2 , may be calculated from the expression

$$\theta_3 = \tan^{-1} \left[\frac{\sin \theta_2 + (2\pi r_2 / \omega_2 C_0 Z_{02} h) \cos \psi_2}{\cos \theta_2 - (2\pi r_2 / \omega_2 C_0 Z_{02} h) \sin \psi_1} \right] \quad (8)$$

where

$$\begin{aligned} \theta_i &= \tan^{-1} \left[\frac{N_0(kr_i)}{J_0(kr_i)} \right] \\ \psi_i &= \tan^{-1} \left[-\frac{J_1(kr_i)}{N_1(kr_i)} \right] \\ Z_{0i} &= 377 \left[\frac{J_0^2(kr_i) + N_0^2(kr_i)}{J_1^2(kr_i) + N_1^2(kr_i)} \right]^{1/2} \end{aligned}$$

and $k = \omega/c$, the wave number. J_0 , J_1 , N_0 , N_1 are Bessel functions of the first and second kinds and C_0 is the loading capacitance. The latter is estimated as the sum of four parallel connected capacitances

$$C_0 = C_g + C_h + C_{d1} + C_{d2}. \quad (9)$$

The gap capacitance, C_g , is the equivalent parallel plate capacitance for an area equal to that on a ferrule edge, $\pi(r_2^2 - r_1^2)$, and a separation, g . Thus

$$C_g = \epsilon_0 \pi (r_2^2 - r_1^2) / g. \quad (10)$$

The "hole" capacitance, C_h , is an artifice made by assuming a parallel plate capacitor with area equal to the beam hole area and a separation $L/2$. Then

$$C_h = 2\epsilon_0 \pi r_1^2 / L. \quad (11)$$

The capacitances C_{d1} and C_{d2} are the discontinuity capacitances located at r_1 and r_2 , i.e., where the cavity height changes. For a symmetric step

$$C_{di} = \pi r_i C_d' \quad (12)$$

where the value of C_d' as a function of gap ratio is obtained from a curve in Ramo and Whinnery.⁷ The gap ratio at r_1 is considered to be $2g/L$. (Note that once r_3 is calculated, it may be inserted back into (8) to obtain the higher order cavity mode resonant frequency, ω_3 , corresponding to the TM_{02} mode.) The ratio of upper to lower cutoff

frequency of the operating mode is related to the coupling iris angle α in the following manner.

$$\frac{\omega_2}{\omega_1} = \sqrt{\frac{180}{180 - \alpha}} \quad (13)$$

for α in degrees. The final dimensions of the M4040 cavities are summarized in Fig. 10.

Some insight into the manner in which the slow-wave structure may be matched to rectangular waveguide can be obtained by considering a lumped-element equivalent circuit. One such circuit, suggested by Pierce,⁸ appears in Fig. 12(a). Using the Tee equivalence in Fig. 12(b),

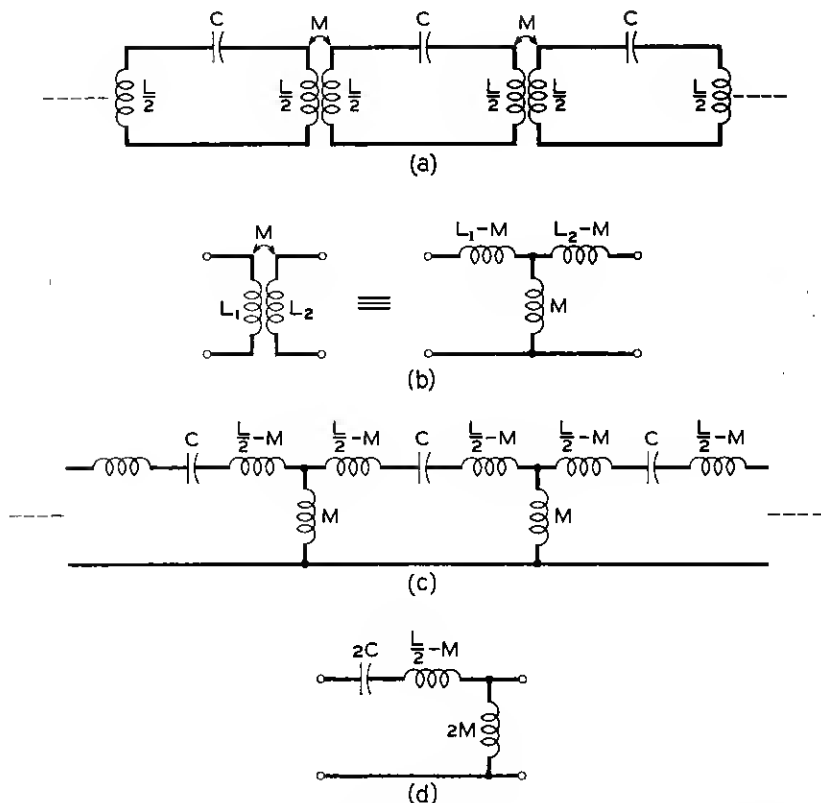


Fig. 12 — (a) Equivalent circuit for a chain of coupled cavities; (b) equivalent Tee circuit for a transformer; (c) transposition of circuit 12(a); (d) half section of circuit 12(c).

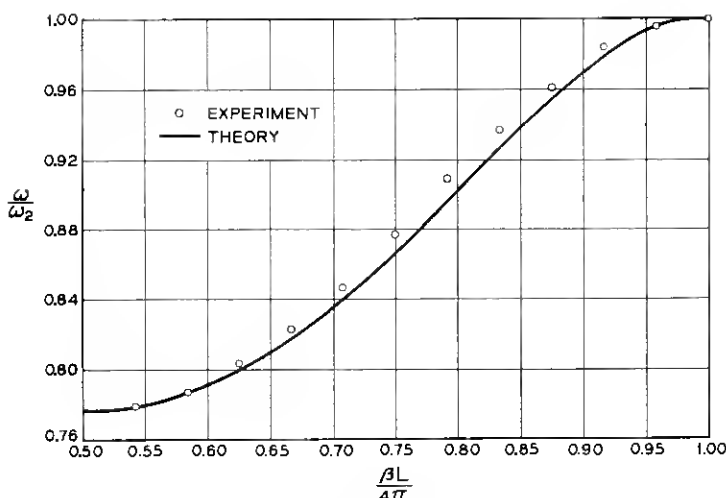


Fig. 13 — Comparison of an experimental ω - β curve with the theoretical dispersion curve of the assumed equivalent circuit.

the circuit of Fig. 12(a) may be transposed to that of 12(c), which in turn has the characteristic half-section of Fig. 12(d). The dispersion curve of this circuit (when the alternation of fields by π radians for adjacent cavities is properly accounted for) is precisely that of (7). Fig. 13 offers a comparison between a typical measured ω - β curve and the theoretical curve from the lumped-circuit approximation. The upper and lower cutoff frequencies are related to the circuit values as shown below.

$$\omega_2 = [C(L - 2M)]^{-\frac{1}{2}} \quad \text{upper cutoff} \quad (14)$$

$$\omega_1 = [C(L + 2M)]^{-\frac{1}{2}} \quad \text{lower cutoff} \quad (15)$$

whence

$$\frac{\omega_2}{\omega_1} = \left[\frac{(L - 2M) + 4M}{(L - 2M)} \right]^{1/2} \quad (16)$$

and

$$\frac{L}{M} = \frac{2(\omega_2^2 + \omega_1^2)}{\omega_2^2 - \omega_1^2}. \quad (17)$$

The equivalent circuit for the last two cavities and the terminating waveguide is represented in Fig. 14(a). The values L , C , and M define

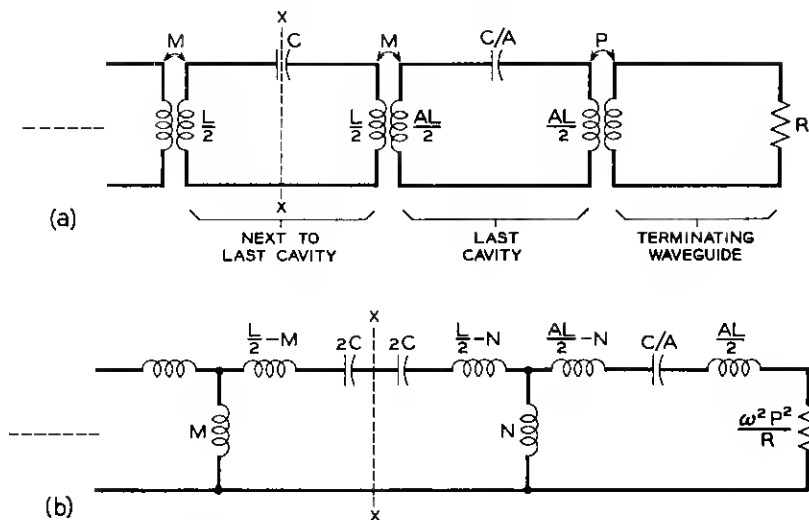


Fig. 14 — (a) Equivalent circuit of terminating cavities and waveguide; (b) transposition of circuit 14(a).

the general cavity circuit and the mutual coupling as before; the coupling between the last two cavities and between the last cavity and the waveguide, however, has been allowed to change to N and P , respectively. The inductance and capacitance of the last cavity have been modified by the factors A and $1/A$, which is roughly equivalent to changing the axial dimensions of the cavity by the factor A . We will assume the inductance of the waveguide termination is negligible. Again applying the circuit equivalence of Fig. 12(b), we arrive at the circuit of Fig. 14(b). Referring to the reference plane x - x , the impedance looking back to the left into the semi-infinite cavity chain is just the Tee impedance of the half-section circuit of Fig. 12(d)

$$Z_T = \sqrt{\omega^2 M^2 - \frac{K^2}{4}} \quad (18)$$

where

$$K = \omega L - \frac{1}{\omega C} = \frac{\omega^2 LC - 1}{\omega C}.$$

The impedance looking to the right of the reference plane can be written

$$Z_R = \frac{R(\omega^2 NP)^2}{(\omega P)^4 + (RAK)^2} + j2K \left[\frac{(\omega P)^4 + (RAK)^2 - 2A(\omega NR)^2}{(\omega P)^4 + (RAK)^2} \right]. \quad (19)$$

Z_R will be real if

$$(\omega P)^4 + (RAK)^2 = 2A(\omega NR)^2 \quad (20)$$

so that

$$R = \frac{(\omega P)^2}{2A \sqrt{\frac{(\omega N)^2}{2A} - \frac{K^2}{4}}}. \quad (21)$$

Substituting (20) and (21) back into (19) and equating Z_R to Z_T , we get

$$\sqrt{\omega^2 M^2 - \frac{K^2}{4}} = \sqrt{\frac{\omega^2 N^2}{2A} - \frac{K^2}{4}} \quad (22)$$

or

$$N = \sqrt{2A} M. \quad (23)$$

Let us assume that we may choose

$$P = \sqrt{B} M \quad (24)$$

where \sqrt{B} is a constant. Then we have

$$R = \frac{B}{A} \left[\frac{(\omega M)^2}{2 \sqrt{\omega^2 M^2 - \frac{K^2}{4}}} \right] \equiv \frac{B}{A} R_0. \quad (25)$$

For convenience the height of the last cavities in the M4040 was left unchanged. This implies that $A = 1$ and that $(L - 2M)$ in (16) is a constant quantity. Combining (13) and (16) with the above constraints yields a prediction for the coupling iris size for N of

$$\alpha_N = 180^\circ \left[\frac{5.656}{L/M + 3.656} \right]. \quad (26)$$

Using $L/M = 8.09$ for the M4040, a figure evaluated from (17), we predicted a value of $\alpha_N = 86.7^\circ$, whereas the empirically determined angle turned out to be 92° .

An inherent difficulty arises when attempting to calculate R_0 , since

(14) and (15) define three circuit values, L , C , and M , in terms of only two known parameters, ω_1 and ω_2 . It remains then to select a suitable reference surface in the cavity in order to estimate one of the lumped-circuit values at that surface. The appropriate surface would seem to be a cylinder, concentric with the cavity, whose radius bisects the coupling iris since the waveguide impedance is presented to the final cavity in this region. The capacitance at this surface may be estimated by making an impedance transformation of the capacitance C_0 , calculated in (9) through (12), over the radial waveguide from radius r_2 to $(r_3 - a/2)$. The calculation of R_0 may be simplified if the midband frequency is chosen as the mean of the cutoff frequencies ($\omega_M = \sqrt{\omega_1\omega_2}$). Combining (14), (15) and (25), one obtains

$$R_0 = \frac{(\omega_2 - \omega_1)(\omega_2 + \omega_1)^2}{16C(\omega_1\omega_2)^2}. \quad (27)$$

The resultant value for R_0 is 3.01 ohms. Since the midband impedance (on a voltage-current basis) of the reduced-height waveguide is 93.5 ohms, P is required to be

$$P = \sqrt{B} M = \sqrt{\frac{93.5}{3.01}} M.$$

Using the same procedure as when calculating α_N , we arrive at a predicted value of $\alpha_P = 141.7^\circ$. The experimentally determined value is 132° .

Experimentally it was also found necessary to increase the ferrule separation in the last two cavities in direct proportion to the sum of the coupling iris angles on the two end walls of the cavity. Identical transition sections are used for input, output and sever waveguides. A typical curve of reflection coefficient versus frequency is shown in Fig. 15.

Considering the devious nature of the above calculations, plus all the usual inadequacies of a lumped-circuit approximation, the predicted and experimental values of iris angles show reasonable agreement. The equivalent circuit approach is valuable, however, even when it discloses only the qualitative aspects of the matching technique.

VI. METHODS USED TO INHIBIT OSCILLATION

The ω - β diagram, Fig. 11, shows the higher-order modes associated with the coupled cavity slow-wave structure. At the cutoff frequencies for these, as well as the fundamental mode, there is a substantial prob-

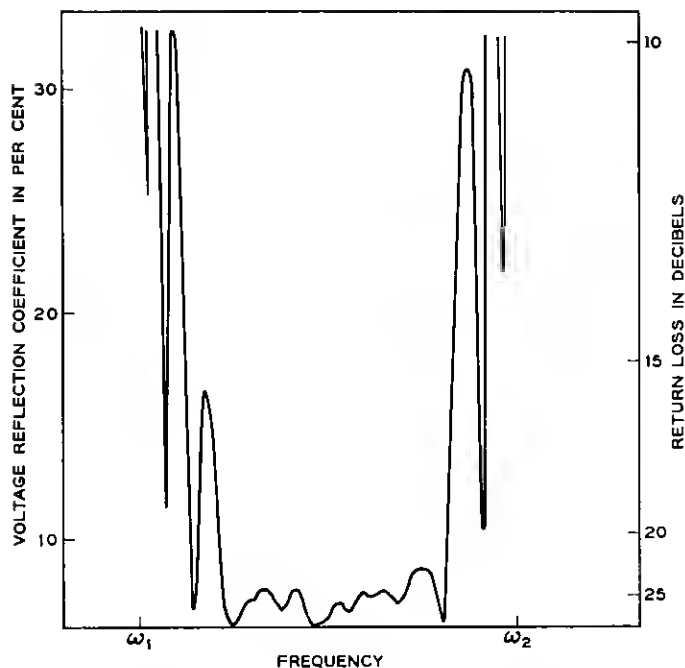


Fig. 15 — Reflection coefficient vs frequency looking into a single section of the slow-wave circuit.

ability that the tube will oscillate if the corresponding wave phase velocities lie close to the electron beam velocity. The intersection of the line, in Fig. 11, labeled "operating voltage" with any of the ω - β plots indicates a synchronism of the wave velocity, for the corresponding mode, with the beam velocity. The slope of the "operating voltage" line is proportional to the electron velocity. Thus, it may be seen that as the beam voltage is raised from 0 to the operating value, synchronism at a cutoff frequency can occur for many modes. The magnitude of the interaction impedance for these modes will determine whether oscillation can occur, and at the cutoff frequency this magnitude may be very large. Oscillations have definitely been identified at 7.1 gc, 12.7 gc and 17.1 gc and at voltages as low as 4 kv and as high as 18 kv. Several techniques have been used to inhibit and avoid the oscillations.

For normal operation, the beam is intended to interact with the first forward wave harmonic of the lowest-order mode. As the beam voltage is raised toward the operating value, the tube will break into a very

strong oscillation at the upper cutoff frequency of 7.1 gc. If one attempts to raise the voltage through the oscillation range with full beam power available, the tube will gas up; arcing will occur; and the beam supply will shut off. Since the Philips cathode can be run at full voltage under temperature-limited conditions, the following turn-up method was used. The cathode temperature is lowered until it is capable of emitting only 15 per cent of full current. The strength of the oscillation under these conditions will be greatly reduced. The beam voltage may now be turned up through the oscillating range to the operating point. Finally, the cathode temperature is returned to its normal value, resulting in full beam power at the operating point. After the tube is sufficiently aged in, the full beam power of 17.7 kilowatts can be applied abruptly by means of a vacuum relay connecting the tube to the power supply.

The original version of the slow-wave circuit had a kidney-shaped cavity coupling slot (cavity A in Fig. 11). The operating voltage line cut the phase-frequency curve for the first higher-order mode (slot-mode) at a high impedance point near the upper cutoff. Oscillation occurred at 12.7 gc. Fig. 11 shows that by capacity-loading the slot to produce the dumbbell shape (cavity B), the mode is lowered in frequency without affecting the operating mode. The impedance of the slot-mode decreases toward the low-frequency end of its passband. Therefore, the elimination of the slot-mode oscillation was accomplished by lowering its frequency until the operating voltage line intersected the phase-frequency curve for the slot-mode at a low impedance point.

A better understanding of the nature of the slot-mode can be obtained from the following analysis. It is assumed that the effects of the ferrule are merely to lower the various passband frequencies since it is placed in a region of large electric fields. This should not affect the slot-mode too greatly. A further assumption is that there is no reaction between slots, which will be nearly true if there is a 180-degree rotation from slot to slot. One may consider the coupled-cavity circuit as a TM_{01} circular waveguide of characteristic impedance Z_{01} and propagation constant β_{01} shunted by a normalized reactance jx corresponding to the circular end walls which form the cavities. If we treat a section, l , of this guide as a TEM transmission line, the eigenvalue equation is given by⁹

$$\cos \theta = \cos \beta_{01}l + \frac{1}{2x} \sin \beta_{01}l \quad (28)$$

where θ is the phase shift per section. The band edge frequencies may be solved for by setting $\theta = 0$ and $\theta = \pi$. For $\theta = 0$

$$\cot \frac{\beta_{01}l}{2} = 2x \quad \text{or} \quad \sin \frac{\beta_{01}l}{2} = 0, \quad \text{i. e.,} \quad \beta_{01}l = 0, 2\pi, 4\pi, \dots$$

For $\theta = \pi$

$$\tan \frac{\beta_{01}l}{2} = -2x \quad \text{or} \quad \cos \frac{\beta_{01}l}{2} = 0, \quad \text{i. e.,} \quad \beta_{01}l = \pi, 3\pi, \dots$$

If the periodic spacing, l , is small compared to a wavelength at the TM_{01} frequency, $\beta_{01}l = \pi, 2\pi \dots n\pi$ will occur only at much higher frequencies. Thus, at $\theta = 0$

$$\cot \frac{\beta_{01}l}{2} = 2x \quad \text{or} \quad \beta_{01}l = 0; \quad (29)$$

at $\theta = \pi$

$$-\tan \frac{\beta_{01}l}{2} = 2x \quad (30)$$

where

$$(\beta_{01})^2 = \left(\frac{\omega}{c}\right)^2 - \left(\frac{\omega_2}{c}\right)^2 \quad (31)$$

and ω_2 is the cutoff frequency for the TM_{01} mode.

If the form of the reactance x can be determined, we can solve (29) to (31) for the band edge frequencies. For the TM_{01} mode in circular guide, an inductor would appear as a circular disc with a sector removed, while a capacitor would appear as a circular disc with an annular slot. The large slots generally used might be represented by a parallel LC circuit such that

$$x = \frac{\omega L}{1 - \left(\frac{\omega}{\omega_s}\right)^2} \quad (32)$$

where $\omega_s^2 = 1/LC$ the slot resonant frequency.

It is necessary to make an estimate of L and C and then solve (29) to (31) graphically. In the case of the M4040, the change to the dumb-bell-shaped slot increased the slot capacity without changing the inductance. Thus, the main mode would not be much affected because its bandwidth is mainly determined by the slot inductance. However, ω_s/ω_2 is diminished, lowering the slot-mode passband center frequency and decreasing the ratio of upper to lower cutoff frequency in the slot-mode.

From the above discussion, one concludes that (i) the slot-mode is a perturbed TM_{01} mode; (ii) because of this, rotation of the slots (avoiding slot-to-slot coupling) would not be expected to change the slot-mode passband; and (iii) neither the upper nor the lower cutoff frequency corresponds to the slot resonant frequency.

The operating mode, high-frequency cutoff oscillation at 7.1 gc may also be "drive-induced." That is, when the input signal power (the drive level) is sufficiently high, the electron velocity can be reduced, by conversion of kinetic to microwave energy, to the point where it is again synchronous with the phase velocity corresponding to the 7.1-gc cutoff. Since this occurs at full beam power and the oscillation is very strong, it is necessary to limit the signal input level to prevent possible tube damage.

VII. ASPECTS OF TUBE PERFORMANCE

Figs. 16 to 22 are plots of power, gain and interception currents as functions of frequency, magnetic field, etc., for various parameter values. They were taken from the performance data of a tube presently located at the Andover station and are believed to be typical of the M4040. Although the graphs are self-explanatory, there are several points worth noting:

(i) The variation of small-signal gain with frequency is similar to that calculated, using the theory of Birdsall and Brewer,¹⁰ except that

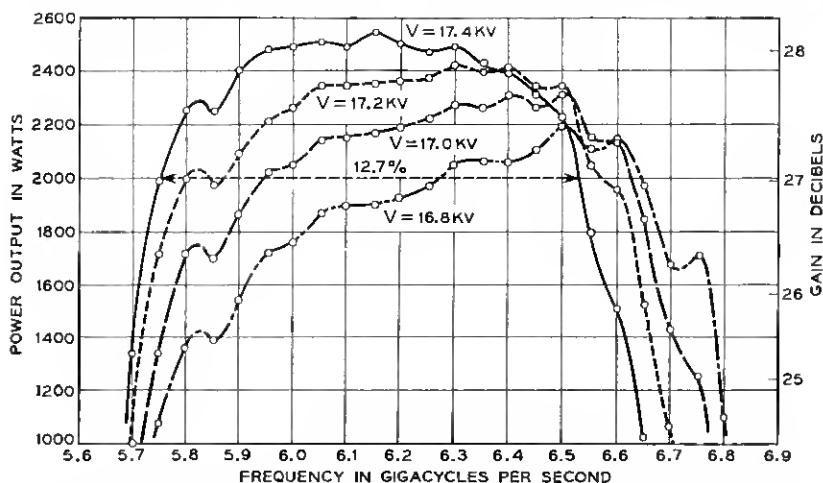


Fig. 16 — High-level output vs frequency [$H = 1.2 \text{ H}$ (Brillouin); power in = 4.2 watts; parameter is beam voltage].

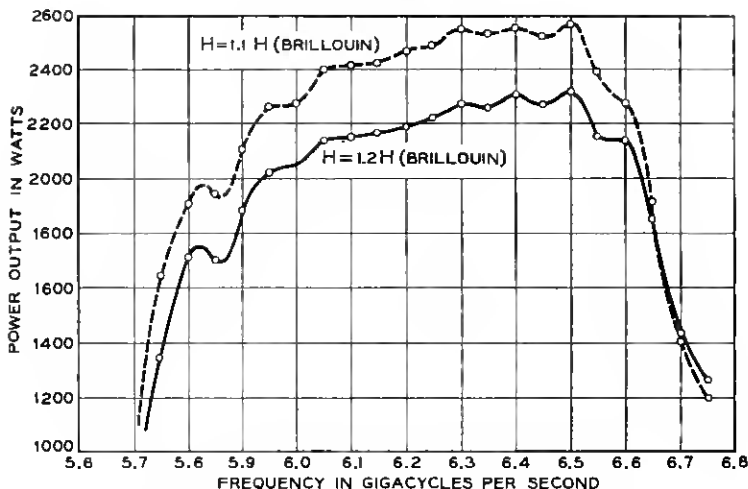


Fig. 17 — High-level output vs frequency [$V = 17.0$ kv; power in = 4.2 watts; parameter is magnetic field].

the tube requires slightly higher voltages than those calculated. The tube must operate at a voltage of 17.4 kv to achieve a gain-frequency curve similar to that calculated for 16.8 kv. (This latter voltage includes the relativistic correction.) The high-level output observed matches that calculated near the center frequency but is in disagreement at the low-

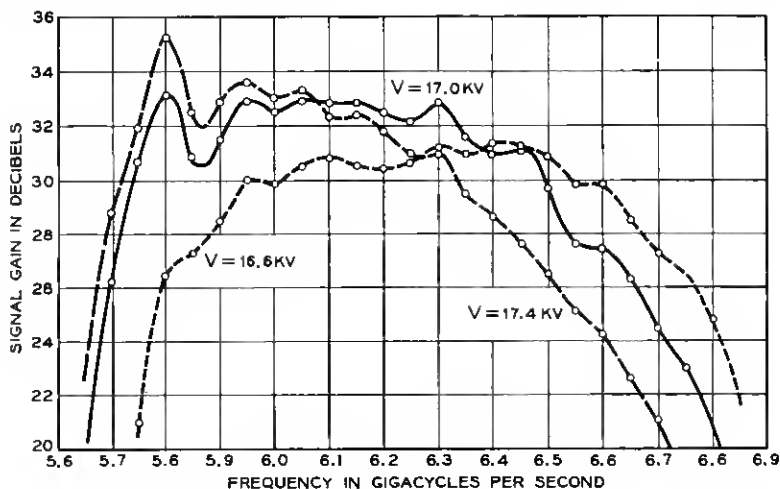


Fig. 18 — Small-signal gain vs frequency [$H = 1.2$ H (Brillouin); parameter is beam voltage].

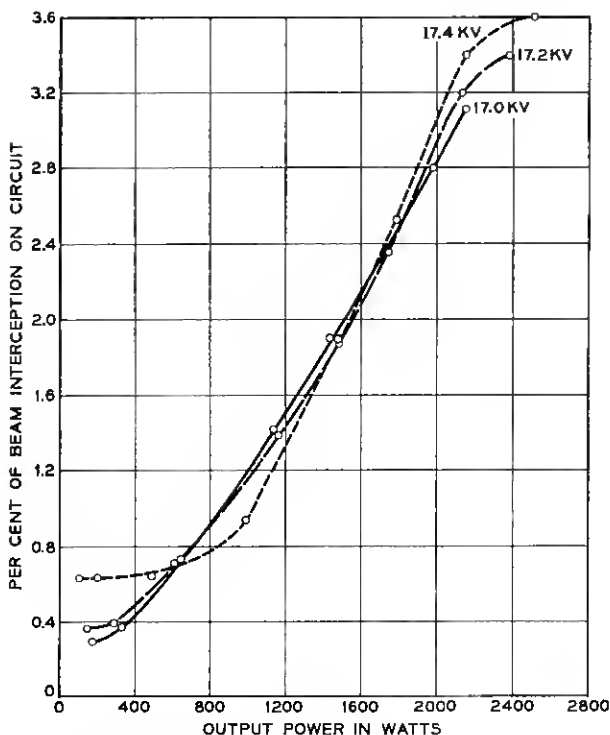


Fig. 19 — Beam interception vs output power [$H = 1.2 H$ (Brillouin); parameter is beam voltage].

frequency end of the band. It is likely that a combination of higher applied voltage and higher input signal power might reproduce the curve shape of sharply rising power with decreasing frequency calculated for 16.8 kv. Here, the experimental data of C. C. Cutler¹¹ were combined with the small-signal calculations of Birdsall and Brewer to predict output power as a function of frequency.

(ii) The M4040 is operated with a focus field value fairly close to the Brillouin magnetic field value. To correlate the several parameters used as a measure of magnetic field, we note that

$$H \text{ (Brillouin)} \approx 600 \text{ oersted}$$

$$H = 1.1 H \text{ (Brillouin)} \approx 660 \text{ oersted} \approx I_{\text{mag}} = 21 \text{ amps}$$

$$H = 1.2 H \text{ (Brillouin)} \approx 720 \text{ oersted} \approx I_{\text{mag}} = 23 \text{ amps.}$$

(iii) The gross "wiggles" in the small-signal gain and high-level out-

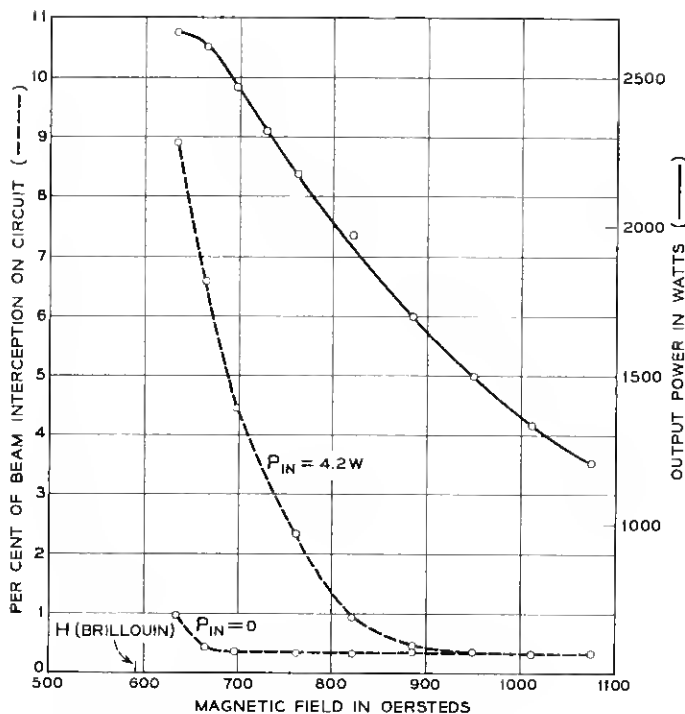


Fig. 20 — Output power and beam interception as a function of magnetic field [$V = 17.0$ kv; $f = 6.4$ gc].

put power versus frequency plots can be correlated with variations in the cold input and output matches.

(iv) The best explanation, at present, for the increase in gain with collector depression is that the resulting ion drainage from the beam allows the latter to expand. The increase in gain is about 1 db for a 300-volt depression. Not much is gained by going to higher potentials. Three hundred volts is about the magnitude of the potential of the beam center relative to the enclosing walls.

Particularly in the tubes produced early in the development period, positive ion effects were noticed. They can neutralize the beam and therefore change its diameter and, with it, the gain. Relaxation effects, much as described by Sutherland,¹² with frequencies dependent on nearly every adjustable parameter were observed. Improved vacuum processing has brought the magnitude of the effects to the point where they are of no concern. Ion effects were observed at an early stage in the electron gun region. It was necessary to maintain the accelerating

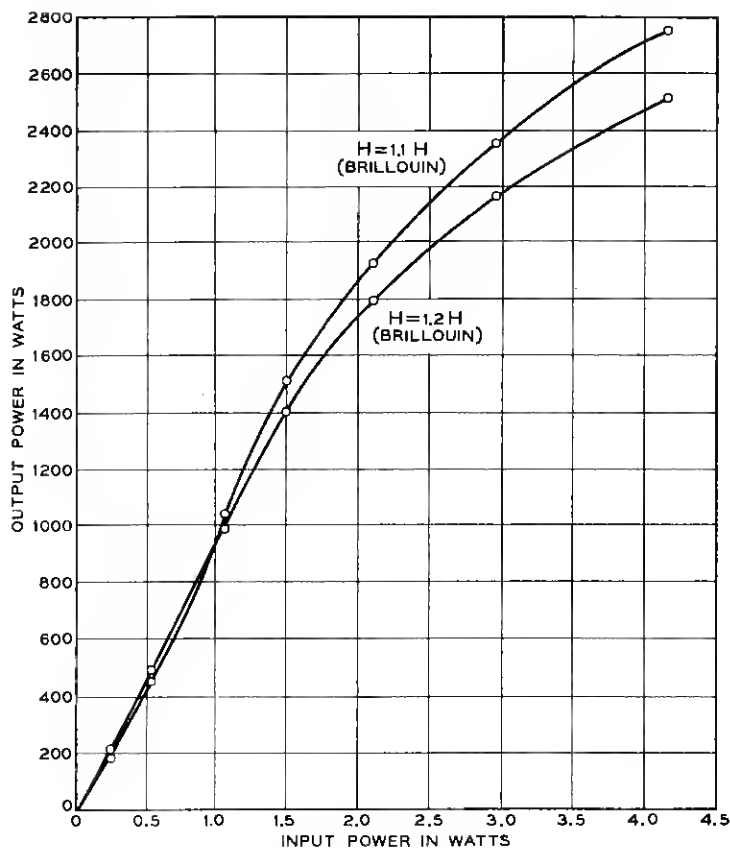


Fig. 21 — Output power vs input power for two values of magnetic field [$V_k = 17.4$ kv; $f = 6.4$ ge; parameter is magnetic field].

electrode positive relative to the slow-wave circuit by about 600 volts. If this voltage is allowed to drop below +450 volts, a poisoning of the cathode takes place, presumably due to ion bombardment.

To convince ourselves that the M4040 would indeed serve as a communications device and do its job in the Telstar system, we set up closed-circuit television apparatus to observe and compare a TV picture first transmitted through a straight waveguide and then transmitted through the M4040 substituted for the waveguide. No observable deterioration of the transmitted picture occurred with the M4040 included. The M4040 was operated over a 30-db range of signal power in these experiments. We also measured the second harmonic output power as

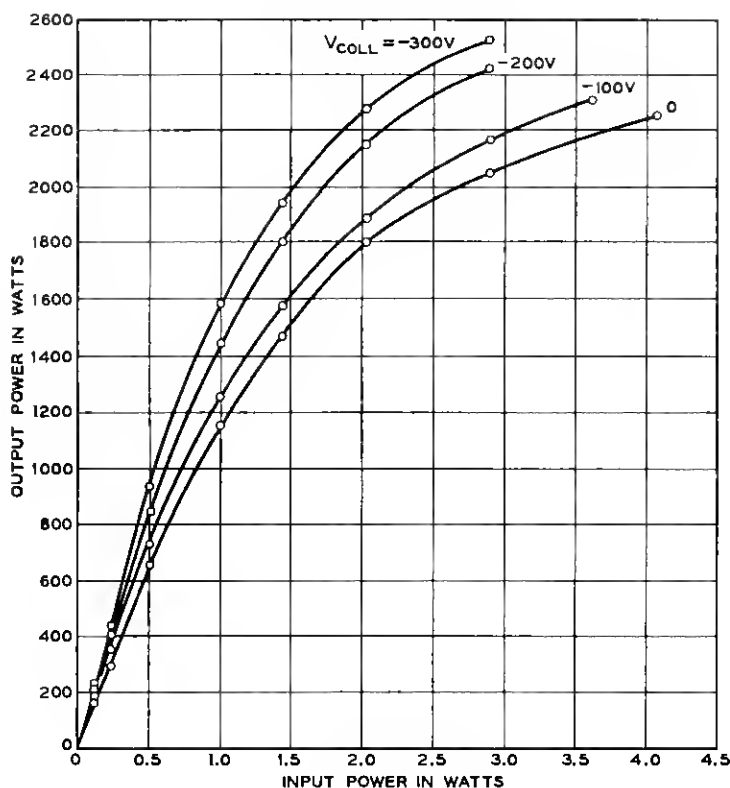


Fig. 22 — Output power vs input power [$V_k = 17.0$ kv; $H = 1.2$ H (Brillouin); $f = 6.4$ gc; parameter is collector depression].

30 db below the output signal level at full output level. With zero applied signal, the noise output is 2 milliwatts as detected through a low-pass filter cutting off at 7.2 gc. Over the narrow, 30-mc bandwidth of the Telstar system, this noise output is 0.4 milliwatt.

VIII. CONCLUDING REMARKS

The M4040 CW traveling-wave tube is capable of operation over a 12.7 per cent bandwidth centered at 6.15 gc with output power exceeding 2000 watts and a gain exceeding 27 db. In the Telstar experiment, the tube has performed satisfactorily as a television transmitter over a 30-db range of input signal power. At the time of writing, both the ground station at Andover, Maine, and the one at Pleumeur Bodou, France, are still using as the power amplifier the original M4040 tubes employed

during the first Telstar broadcasts. The tube at Andover has been operated for approximately 1500 high-power hours.

Recently, several experiments have indicated that much improved performance can be expected from the M4040. Two more cavities have been added to the output section of the tube, increasing the gain. At the midband frequency of 6.15 gc, the small-signal gain becomes 35 db and the gain, at the maximum output power of 2700 watts, is 30 db. Further experiments demonstrated that the water cooling rate could be drastically reduced and that ion drainage could be achieved by applying a negative voltage to a pair of electrodes concentric with the beam. The M4040 has been operated without the aid of appendage pumps after an age-in period of some 50 hours. Finally, and perhaps most significantly, the collector potential has been depressed 9 kv below the potential of the slow-wave circuit.¹³ The resulting over-all tube efficiency becomes greater than 30 per cent, and a relatively unregulated power supply can be used to provide the beam power. The latter benefit is obtained because of the insensitivity of tube performance to collector voltages depressed beyond 400 volts. If one depresses the collector potential below 9 kv, undesirable effects of electrons returning to the gun region from the collector can be observed.

IX. ACKNOWLEDGMENTS

The development of the M4040 is the result of the cooperative efforts of a great many people in the engineering, assembly, and fabrication areas. The authors thank Messrs. J. W. Gewartowski, H. N. Carlson, and F. R. Ashley for allowing the inclusion of information developed during the course of their work on the M4040 traveling-wave tube.

REFERENCES

1. Pierce, J. R., *Theory and Design of Electron Beams*, Van Nostrand, New York, 1954, Chap. 10.
2. Danielson, W. E., Rosenfeld, J. L., and Saloom, J. A., Analysis of Beam Formation with Electron Guns of the Pierce Type, B.S.T.J., **35**, March, 1956, pp. 375-420.
3. Herrmann, G., Transverse Scaling of Electron Beams, J. Appl. Phys., **28**, April, 1957, pp. 474-478.
4. Spangenberg, K. R., Field, L. M., and Helm, R., *Production and Control of Electron Beams*, Federal Telephone and Radio Corp., New York, 1942.
5. Jahnke, E., and Emde, F., *Tables of Functions*, Dover Publications, New York, 1945, p. 32.
6. Ramo, S., and Whinnery, J. R., *Fields and Waves in Modern Radio*, John Wiley and Sons, First Edition, New York, 1944, pp. 406-408.
7. Ibid., p. 376.
8. Pierce, J. R., *Traveling-Wave Tubes*, D. Van Nostrand, New York, 1950, p. 68.

9. Collin, R. E., *Field Theory of Guided Waves*, McGraw-Hill Book Co., New York, 1960, p. 385.
10. Birdsall, C. K., and Brewer, G. R., Hughes Technical Memo, No. 396, June, 1955.
11. Cutler, C. C., The nature of Power Saturation in Traveling-Wave Tubes, *B.S.T.J.*, **35**, July, 1956, pp. 841-876.
12. Sutherland, A. D., Relaxation Instabilities in High Perveance Electron Beams, *I.R.E. Trans. on Electron Devices*, ED-7, October, 1960, p. 268-273.
13. Melroy, D. O., private communication.

